







NIS-SLAM: Neural Implicit Semantic RGB-D SLAM for 3D Consistent Scene Understanding

Hongjia Zhai , Gan Huang , Qirui Hu , Guanglin Li , Hujun Bao , and Guofeng Zhang 

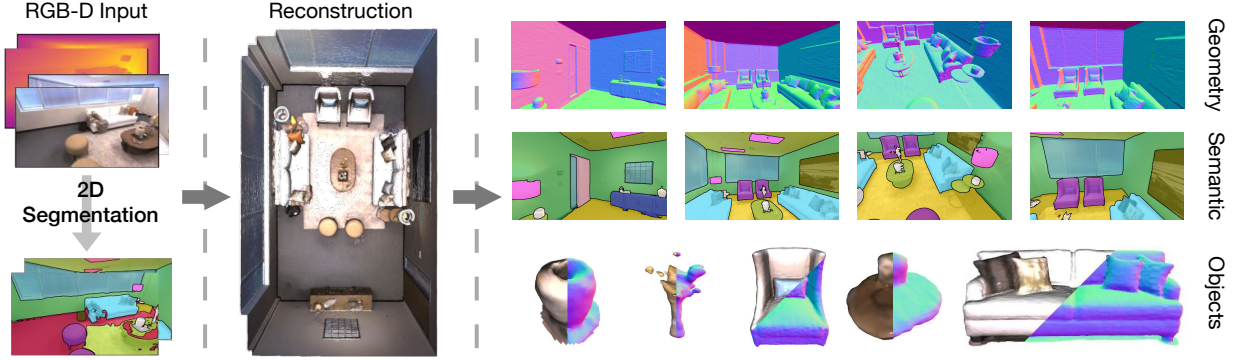


Fig. 1: We present NIS-SLAM, a neural implicit semantic RGB-D SLAM system that incrementally reconstructs the environment with 3D consistent scene understanding. As shown in the figure, taking continuous RGB-D frames and 2D noise segmentation results as input, our system can reconstruct high-fidelity surface and geometry, learn 3D consistent semantic field, and recover the objects in the scene.

Abstract—In recent years, the paradigm of neural implicit representations has gained substantial attention in the field of Simultaneous Localization and Mapping (SLAM). However, a notable gap exists in the existing approaches when it comes to scene understanding. In this paper, we introduce NIS-SLAM, an efficient neural implicit semantic RGB-D SLAM system, that leverages a pre-trained 2D segmentation network to learn consistent semantic representations. Specifically, for high-fidelity surface reconstruction and spatial consistent scene understanding, we combine high-frequency multi-resolution tetrahedron-based features and low-frequency positional encoding as the implicit scene representations. Besides, to address the inconsistency of 2D segmentation results from multiple views, we propose a fusion strategy that integrates the semantic probabilities from previous non-keyframes into keyframes to achieve consistent semantic learning. Furthermore, we implement a confidence-based pixel sampling and progressive optimization weight function for robust camera tracking. Extensive experimental results on various datasets show the better or more competitive performance of our system when compared to other existing neural dense implicit RGB-D SLAM approaches. Finally, we also show that our approach can be used in augmented reality applications. Project page: https://zju3dv.github.io/nis_slam.

Index Terms—Implicit representation, Neural dense SLAM, Semantic segmentation, Scene understanding

1 INTRODUCTION

Dense Simultaneous Localization and Mapping (SLAM) is a fundamental research topic in 3D computer vision, which aims to localize the 6 degrees of freedom (6DoF) pose of the camera and reconstruct a dense map in an unknown environment. It is an essential part of Virtual/Augmented Reality (VR/AR), robot localization/navigation, and visual perception. For example, in VR/AR, the SLAM system can provide pose information for mobile devices and head-mounted devices to help users interact with virtual content, and the geometric results of dense reconstruction can better simulate physical space collisions, thereby creating a better immersive and engaging experience.

Traditional RGB-D SLAM [13, 42, 68] usually performs frame-to-model optimization to track camera based on the pixel-level depth or color observations from RGB-D camera. Benefit from the depth sensor, traditional approaches use iterative closest points (ICP) [1] and truncated signed distance function (TSDF) [11] to update a global map represented by geometric primitives, such as voxels, cost volumes, and surfels. With the development of deep learning, recent works have

turned to exploring data-driven priors and leveraging the smoothness properties of neural networks [3, 20, 29, 62, 66]. Although traditional and learning-based dense SLAM systems have shown good localization and reconstruction performance, they cannot perform novel view rendering and produce watertight surfaces. For VR/AR applications, realistic image rendering and novel view synthesis also play an important role.

As one of the research fields, Neural Radiance Field (NeRF) based SLAM methods [23, 50, 58, 64] have shown significant advantages in novel view rendering, high-fidelity map reconstruction, and hole filling. Different from the traditional SLAM approaches, neural implicit SLAM uses a neural radiance field to represent scene property and uses multilayer-perceptron (MLP) to decode the attributes of the scene (color, density, signed distance function, semantic information, etc.). Benefiting from volume rendering [24] and positional encoding [37], implicit representation enables high-fidelity image rendering and new perspective synthesis. iMAP [58] is the first neural implicit dense SLAM, which directly uses a single MLP to model the geometry and appearance information. However, it is hard to reconstruct large indoor scenes due to the forgetting problem of MLP in continual learning. To overcome this challenge, many works propose to use additional parametric encoding, like dense feature grid/plane/point [23, 50, 71, 78, 79], hash table [17, 22, 64], to increase the representation ability of the MLP. However, additional dense features will lead to more memory usage, which is not efficient. Besides, semantic information also plays an important role in SLAM, which allows robots to perceive and understand the world. Although there exist works [14, 28, 54, 74]

- Hongjia Zhai, Gan Huang, Qirui Hu, Guanglin Li, Hujun Bao, and Guofeng Zhang are with the State Key Lab of CAD&CG, Zhejiang University, Hangzhou 310058, China. E-mails: {zhj1999, huanggan, 3200105912, liguanglin, baohujun, zhangguofeng}@zju.edu.cn.
- Corresponding Author: Guofeng Zhang.

that combine neural implicit representation and semantics modeling, little attention has been paid to modeling semantic information in a neural implicit dense SLAM. This is because using neural implicit representation to simultaneously perform camera tracking and semantic learning with inconsistent 2D semantic input is rather challenging.

vMAP [26] and Haghighi *et al.* [17] are the most related works that use implicit representation to model 3D instance/semantic information. vMAP [26] uses ground truth pose and instance mask for commonly used datasets [12, 55] to reconstruct the object in the scene. Haghighi [17] uses ORB-SLAM3 [5] to provide pose for the mapping process and they ignore the inconsistency problem of 2D segmentation. Using the traditional SLAM approach as a decoupled front end makes them turn into a mapping method instead of an SLAM method. Besides, they don't handle the problem of camera pose estimation and multi-view inconsistency of 2D segmentation. As mentioned above, currently, there is no implicit-based approach that simultaneously performs camera tracking, dense surface reconstruction, and 3D consistent scene semantic understanding from noisy 2D input.

To this end, in this paper, we introduce NIS-SLAM, an efficient neural implicit semantic RGB-D SLAM system, which enables simultaneous scene reconstruction and learning 3D consistent semantics from the inconsistent segmentation results of 2D CNN. Specifically, for high-fidelity surface reconstruction and spatial consistent scene understanding, we use the hybrid representation of high-frequency multi-resolution tetrahedron-based features and low-frequency positional encoding as the input of our system. Besides, to learn a 3D consistent semantic field, an effective multi-view semantic fusion strategy is introduced to handle the inconsistency of 2D segmentation results. Finally, semantic-guided pixel sampling and progressive optimization weight are also used for robust camera tracking. In summary, our contributions include:

- We propose an efficient neural implicit semantic RGB-D SLAM system with hybrid implicit representation. Our system can simultaneously reconstruct the environment and model 3D consistent semantic information from 2D segmentation results.
- We propose an effective multi-view semantic fusion that enables learning 3D consistent semantic information. Besides, semantic guided sampling and progressive optimization weight are used for robust camera tracking.
- We perform extensive experiments on commonly used datasets to demonstrate the state-of-the-art and comparable performance of camera tracking, reconstruction, and semantic segmentation.

This paper is structured as follows: In Sec. 2, we provide a review of related works to contextualize our research. Next, in Sec. 3, we explain each key component in our reconstruction pipeline. Subsequently, in Sec. 4, we evaluate the performance of our system through various synthetic and real-world datasets. Finally, conclusion is given in Sec. 5.

2 RELATED WORK

2.1 Dense Visual SLAM

DTAM [43] was the first dense SLAM system that leveraged pixel-level photometric information to perform camera pose tracking. Taking advantage of RGB-D cameras, some traditional approaches use iterative closest points (ICP) [1] and truncated signed distance function (TSDF) [11] to achieve good 3D reconstruction results, such as KinectFusion [42], BundleFusion [13], and ElasticFusion [69]. Benefiting from deep learning technology, some learning-based approaches [3, 20, 59, 61, 62, 66] are proposed to improve the robustness and accuracy. For example, DI-Fusion [20] and CodeSLAM [3] learn the scene representation implicitly which encodes the geometry information in a low dimensional latent feature. BAD-SLAM [51] uses a direct bundle adjustment (BA) to jointly optimize the poses of keyframe and 3D scene geometry. There are still some approaches that pay attention to scene understanding, like SemanticFusion [36] and PanopticFusion [41]. Besides, semantic-based object alignment [18] and reconstruction [16] also play an important role in robot navigation and perception. Although these methods use learning-based components, the scene and map representation of the environment and the

system framework are still the same as traditional SLAM methods. They cannot achieve realistic image rendering and novel view synthesis, which is more important for the applications of VR/AR.

2.2 Neural Implicit Scene Representation

Implicit representation has facilitated novel applications in 3D computer vision, such as novel view synthesis [37, 60, 63], surface reconstruction [2, 7, 30, 44, 65], and dynamic scene reconstruction [15, 45–47]. Depending on the scene representation approaches, three main categories emerge: network-based, grid-based, and point-based. Network-based methods [2, 35, 37, 46, 65] offer a continuous representation of the scene through implicit modeling via coordinate MLPs, enabling rendering and surface reconstruction. However, due to the limited representation capacity of MLPs, they often exhibit reduced efficacy in representing and reconstructing large-scale scenes. Consequently, grid-based approaches have evolved, employing explicit representations like dense grids to encode scene information, partially mitigating the limitations of MLP-based decoding. Additionally, some methods utilize sparse voxels [30–32], hashtables [38, 49], tetrahedron [27, 39, 53] or other efficient representations [6, 23] to reduce the parameters of the grid. Point-based methods [50, 70] allow for a more flexible scene representation, where points can be concentrated near complex surfaces to avoid wasting memory on modeling unused free space. 3D Gaussian Splatting [25] also can be viewed as the point-based method, which uses Gaussian to encode the local information of 3D points in the scene. The splatting strategy avoids dense point sampling along the camera ray, which accelerates the rendering speed of the neural implicit model. However, the overall parameter count for the entire representation is directly proportional to the number of points which usually needs to be at least semi-dense to ensure a relatively good reconstruction performance.

2.3 Neural Implicit Dense SLAM

Recently, there have been successful approaches that combine dense visual SLAM with neural implicit radiance fields [23, 58, 64, 71]. Compared to the traditional SLAM approaches, neural implicit SLAM can reconstruct the watertight surface of the scene and perform realistic novel view rendering. iMAP [58] was the first neural implicit SLAM approach that uses coordinate MLPs to represent the scene and continuously update it during incremental mapping. To address the challenge of reconstructing large indoor scenes, some approaches utilize multi-level dense feature grids [23, 78, 79], hash table [64], and voxel/point embeddings [22, 50, 71, 72] to mitigate the representation ability of coordinate MLPs. Besides, some methods [10, 22, 26, 48, 73] decouple the front and back ends, employing traditional or learning-based VO/VIO [40, 52, 62] for camera pose tracking and utilizing implicit representation in the back end for dense reconstruction. To perform scene understanding, Haghighi *et al.* [17] and vMAP [26] incorporate semantic/instance information into neural implicit reconstruction, which both use ORB-SLAM3 [5] to provide camera pose. Zhu *et al.* [76] propose the first neural semantic mapping system, which learns consistent semantic fields based on the pose estimated by neural SLAM. These kinds of approaches using decoupled modules can accelerate tracking speed and accuracy in complex scenes but depart from a couple of pure implicit SLAMs.

3 METHOD

The pipeline of our method is shown in Fig. 2. Given an input sequence of RGB-D images $\{I_i \in \mathbb{R}^3, D_i \in \mathbb{R}\}$, we first generate the 2D semantic segmentation results $\{S_i\}$ and confidence $\{Conf_i\}$ via a pre-trained CNN model (Mask2Former [9]). Based on those inputs, our system is capable of recovering camera poses, and implicit SDF fields, and additionally reconstructing a 3D consistent semantic representation. These individual components will be explained in detail in the following subsections. We first introduce our tetrahedron-based neural implicit representation (Sec. 3.1) and how color/depth/semantic information is rendered via SDF-based volume rendering (Sec. 3.2). Then, the multi-view semantic fusion strategy is proposed to handle the noise semantic information (Sec. 3.3). Besides, the overall optimization

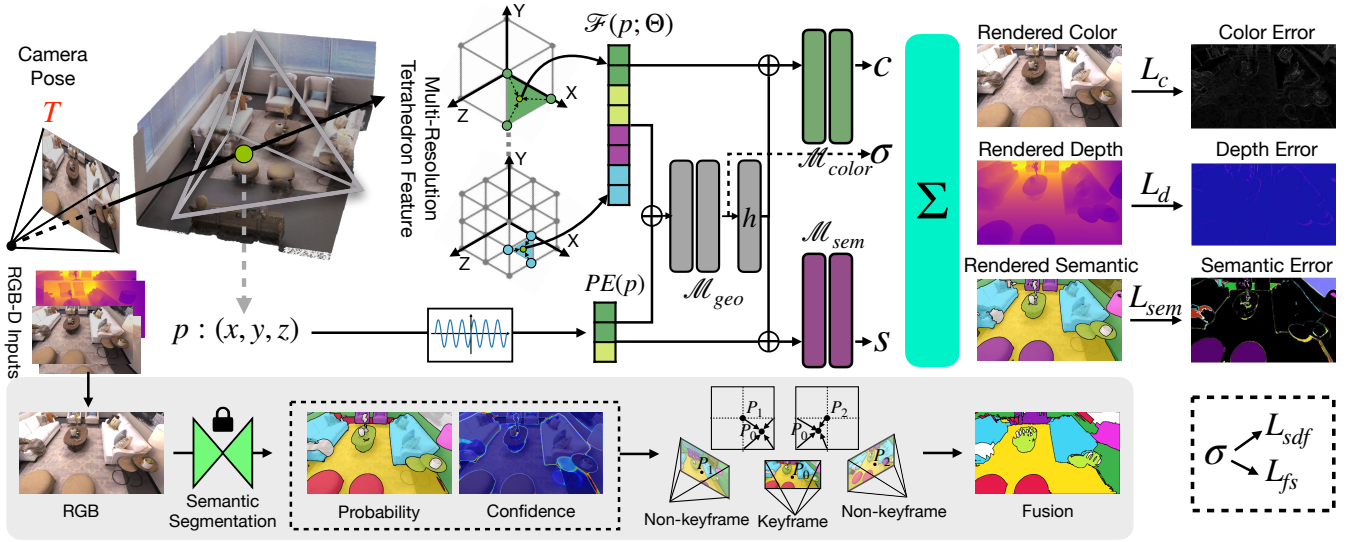


Fig. 2: Our system takes RGB-D frames as input to perform camera tracking and mapping via volume rendering and models 3D semantics with the noise 2D segmentation results from Mask2Former [9]. Based on the hybrid implicit representation of multi-resolution tetrahedron feature θ and positional encoding $PE(p)$, we decode the SDF σ , latent feature h , color c , and semantic probability s with three MLPs $\{\mathcal{M}_{geo}, \mathcal{M}_{color}, \text{ and } \mathcal{M}_{sem}\}$. To model consistent semantic property, we fuse multi-view semantics of nearby non-keyframes for learning 3D consistent representation.

objective functions are introduced in Sec. 3.4. Finally, the tracking and mapping processes of our system are shown in Sec. 3.5 and Sec. 3.6, respectively.

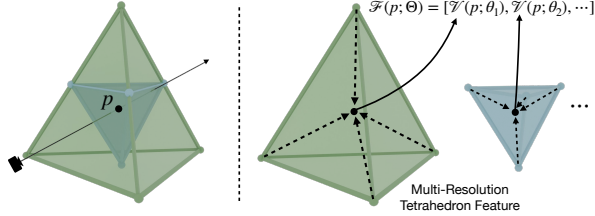


Fig. 3: Barycentric interpolation of multi-resolution tetrahedron feature. For tetrahedrons of different resolutions, we obtain the features of the query point according to the vertex features and barycentric.

3.1 Tetrahedron-based Representation

Only using MLPs [58] to decode the scene property can lead to worse performance due to the forgetting problem during incremental reconstruction of large scenes. Although grid-based or point-based methods [50, 64, 71] can enhance the encoding capacity of MLPs for large indoor scenes, they can not fit the scene surface very well due to the inherent flaws of their representation. Using tetrahedron [27, 53] to encode the scene information is more appropriate than using cube/grid/point due to the fundamental geometric primitive is the triangular face.

Same to [38, 49], we employ a multi-resolution feature to encode high-frequency information (e.g. color) and use a hash table to reduce the additional parameters. Besides, benefiting from the joint encoding [64], we additionally apply a low-frequency positional encoding [37] for reasoning spatial semantics. Additionally, as shown in [4], the semantic information is the low-frequency information compared to the color. So, for semantic property decoding, we concatenate the positional encoding with the latent feature as the input. For color property decoding, we concatenate the tetrahedron feature with the latent feature as the input. Those processes are shown in the top part of Fig. 2.

Specifically, for a 3D point $p \in \mathbb{R}^3$, we first compute its low-frequency positional encoding value $PE(p)$ with following equation:

$$PE(p) = [\gamma(x), \gamma(y), \gamma(z)], \quad (1)$$

$$\gamma(x) = (\sin(2^0 \pi x), \cos((2^0 \pi x)), \dots, \sin(2^{n-1} \pi x), \cos((2^{n-1} \pi x))), \quad (2)$$

where n represents the frequency, and we set $n=8$ in our experiments.

Then, we interpolate the high-frequency feature of p from multi-resolution tetrahedron features $\Theta = \{\theta_l\}_{l=1}^L$. Here, we retrieve multi-resolution tetrahedrons that contain the point p . We obtain its feature via barycentric interpolation according to the feature in the vertexes of the tetrahedrons with the following equation $\mathcal{F}(p; \Theta)$.

$$\mathcal{F}(p; \Theta) = [\mathcal{V}(p, \theta_1), \dots, \mathcal{V}(p, \theta_l)], \quad (3)$$

where $\mathcal{V}(\cdot)$ refers to the barycentric interpolation function for each resolution tetrahedron. The barycentric interpolation of the tetrahedron is shown in Fig. 3. After obtaining the multi-resolution features, we decode the geometry property with geometry MLP \mathcal{M}_{geo} :

$$(h, \sigma) = \mathcal{M}_{geo}(PE(p), \mathcal{F}(p; \Theta)), \quad (4)$$

where h and σ are the latent feature vector and signed distance of location p . Finally, we decode the color and semantic probability based on the latent feature h and input encodings via separated MLPs:

$$c = \mathcal{M}_{color}(\mathcal{F}(p; \Theta), h), \quad s = \mathcal{M}_{sem}(PE(p), h). \quad (5)$$

So, the optimizable parameters for the whole implicit representation are three MLP decoders $\{\mathcal{M}_{geo}, \mathcal{M}_{color}, \mathcal{M}_{sem}\}$ and multi-resolution tetrahedron features Θ .

3.2 SDF-based Volume Rendering

Compared to occupancy or density-based rendering approaches [50, 79], using SDF-based volume rendering can lead to more accurate surface reconstruction. To render color, depth, and semantics for each pixel, we adopt the SDF-based volume rendering strategy [2, 65] to aggregate the property of points along the ray.

Specifically, for ray r emitted from the center of camera with origin $o_r \in \mathbb{R}^3$ and view direction $d_r \in \mathbb{R}^3$, we can sample points along r :

$$p_r(i) = o_r + z_r(i) \cdot d_r, \quad i \in \{1, \dots, M\}, \quad (6)$$

where M is the number of total sampled points, $z_r(i) \in \mathbb{R}$ is the depth of i -th sampled point. Similar to other approaches [23, 64, 79], we replace the importance sampling with a depth-guided sampling strategy. Specifically, we first uniformly sample M_c points between the near and

far bound. We then uniformly sample M_f points around the surface according to the depth values of the selected pixel.

For all $M = M_c + M_f$ points along the ray, we query their signed distance, color, and semantic probability values using MLP decoders (Sec. 3.1). As shown in [2], a simple bell-shaped weight function can be employed to transform the signed distance function, σ , into rendering weights. Here, we adopt the Gaussian distribution with mean 0 as the rendering weight distribution, which is shown as follows:

$$\tilde{w}_i = \frac{w_i}{\sum_j w_j} \quad \text{with} \quad w_i = \frac{1}{\delta\sqrt{2\pi}} \exp(-\sigma_i^2/\delta^2), \quad (7)$$

where δ is the parameter, which controls the shape of the weight distribution for points with different signed distance values. \tilde{w}_i is the normalized rendering weight for i -th point.

So, for ray r , we can obtain its scene property via:

$$\hat{c} = \sum_{i=1}^M \tilde{w}_i c_i, \quad \hat{d} = \sum_{i=1}^M \tilde{w}_i d_i, \quad \hat{s} = \sum_{i=1}^M \tilde{w}_i s_i. \quad (8)$$

3.3 Multi-view Noisy Semantic Fusion

Due to the inherent noise and multi-frame inconsistencies of results generated by Mask2Former [9], the SLAM system may learn wrong 3D semantic representations when the segmentation results of keyframes are inaccurate. Inspired by the warp strategy [67, 75], we propose an efficient approach to fuse semantic information from multi-view frames to address the inconsistency issue. At the bottom of Fig. 2, we first back project the pixel, P_t , of keyframe I_t into k previous non-keyframes I_{t-i} ($i = \{1, \dots, k\}$) according to the relative pose, $T_{t-i \rightarrow t}$, estimated by our neural implicit SLAM system. Then, we synthesize the projected semantics via the differentiable bilinear sampling proposed in [21]. The formula is shown in the following:

$$S_{t-i \rightarrow t} = \text{interp}(K T_{t-i \rightarrow t} D_t K^{-1} P_t, S_{t-i}), \quad (9)$$

where interp denotes the differentiable bilinear sampling operation, K is the camera intrinsics matrix, and $S_{t-i \rightarrow t}$ is the semantic probability projected from I_{t-i} .

Thus, we can obtain the fused semantic information for keyframe I_t from adjacent k non-keyframes. Since 2D segmentation is often accompanied with confidence, we fuse multi-view semantic information based on the normalized confidence weight with Softmax function:

$$S_t^m = \sum_i^k \text{softmax}(\text{Conf}_{t-i}) \cdot S_{t-i \rightarrow t}, \quad (10)$$

where Conf_{t-i} is the confidence of I_{t-i} , and S_t^m is the multi-view fused semantic probability, which can be used as the supervision of semantic MLP.

3.4 Objective Functions

We perform camera tracking and bundle adjustment via objective function minimization. Like [2, 71], to optimize the whole system, we apply five different objective functions: reconstruction loss, SDF loss, free space loss, semantic loss, and regularization loss.

Reconstruction loss. For each ray with ground truth depth and color, we apply the reconstruction losses between the rendered value and ground truth value measured by the camera:

$$\mathcal{L}_c = \frac{1}{|R|} \sum_{r \in R} (\hat{c}(r) - I(r))^2, \quad \mathcal{L}_d = \frac{1}{|R|} \sum_{r \in R} (\hat{d}(r) - D(r))^2, \quad (11)$$

where R is the set of sampled pixels for optimization, $\{I(r), D(r)\}$ are the color and depth value of ray r , and $\{\hat{c}(r), \hat{d}(r)\}$ are the rendered value of sampled ray r , which are computed by Eq. (8).

SDF and free space loss. Apart from the reconstruction loss, we also consider the geometrical information to supervise the reconstruction process. To learn a better geometry representation, we apply constraints

on the signed distance value, σ , with the following SDF loss and free space loss. For the points near the surface and within the truncation region, e.g. $|\hat{d}(p) - D(r)| < tr$, we use depth measurement to approximate the signed distance value:

$$\mathcal{L}_{sdf} = \frac{1}{|R|} \sum_{r \in R} \frac{1}{|P_r^{tr}|} \sum_{p \in P_r^{tr}} (\hat{d}(p) + \sigma \cdot tr - D(r))^2, \quad (12)$$

where tr is the truncation distance, P_r^{tr} is the set of sampled points within the truncation region. The SDF loss \mathcal{L}_{sdf} pushes the signed distance function to fit the surface of the scene.

Besides, for sampled points that are far away from the surface, e.g. $|\hat{d}(p) - D(r)| > tr$, we apply a regularization on the free space that pushes its signed distance to 1:

$$\mathcal{L}_{fs} = \frac{1}{|R|} \sum_{r \in R} \frac{1}{|P_r^{fs}|} \sum_{p \in P_r^{fs}} (\sigma - 1)^2, \quad (13)$$

where P_r^{fs} is the set of sampled points within the free space. The free space loss \mathcal{L}_{fs} pushes the signed distance value of empty space to 1, which reduces the noise or redundant points during the marching cubes.

Semantic loss. To learn a consistent semantic field, we simultaneously use single-view predicted probability and the fused multi-view semantic probability as the supervision for the semantic decoder. Here, we stop the gradient propagation from the semantic MLP to geometry MLP for stable geometry learning. The semantic loss is defined as:

$$\mathcal{L}_{sem} = -\frac{1}{|R|} \sum_{r \in R} \sum_{i=0}^{N_c} [(S_r(i) + \alpha \cdot S_r^m(i)) \log \hat{s}_r(i)], \quad (14)$$

where N_c is the number of classes for semantic segmentation, $S_r, S_r^m \in \mathbb{R}^{N_c}$ are the single-view and fused multi-view semantic probability for ray r , respectively. α is the weight parameter that balances two semantic components.

Regularization loss. Unlike [58] the built-in smoothness priors, which uses a single MLP to represent the scene. To ensure the smoothness of the tetrahedron feature space and to avoid hash collisions when sampling vertex features, we apply regularization on the interpolated multi-resolution features:

$$\mathcal{L}_{reg} = -\frac{1}{|R|} \sum_{r \in R} (\mathcal{F}(p; \Theta) - \mathcal{F}(p + \varepsilon; \Theta))^2, \quad (15)$$

where ε denotes the small perturbation of point location in 3D space, and $\mathcal{F}(\cdot; \Theta)$ is the feature query functions in Sec. 3.1. We only perform the regularization term of the multi-resolution tetrahedron feature during the mapping process on small random regions.

So, the final loss function is presented as follows:

$$\mathcal{L} = \lambda_1 \mathcal{L}_c + \lambda_2 \mathcal{L}_{depth} + \lambda_3 \mathcal{L}_{fs} + \lambda_4 \mathcal{L}_{sdf} + \lambda_5 \mathcal{L}_{sem} + \lambda_6 \mathcal{L}_{reg}, \quad (16)$$

where $\{\lambda_i\}$ are the weight for each optimization component.

3.5 Tracking

For camera tracking, we fix the pose of the first frame as the identity matrix. And for later coming frame I_t , we first initialize its camera-to-world pose, $T_{wc}^t = \exp(\xi) \in \mathbb{SE}(3)$, under the simple constant speed assumption. Then we sample M_t pixels across the frame for pose optimization. During the tracking process, we fix the parameters of decoders and multi-resolution tetrahedron features and only update T_{wc}^t .

Semantic-guided Pixel Sampling. For pixel sampling, we use confidence values from the semantic segmentation as the sampling probabilities for pixels. Pixels with higher confidence values are deemed more reliable for camera tracking compared to those with lower confidence. As shown in Fig. 4, we show the confidence map (left part) and tracking error map of all pixels (right part). Edge and challenge regions usually have low segmentation confidence and high tracking errors due to sensor noise and slow convergence speed of SDF filed in

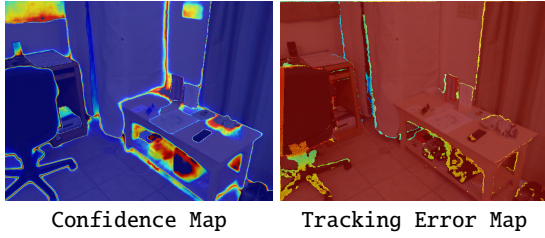


Fig. 4: Segmentation confidence map and tracking error map. Complex geometry and ambiguous regions usually lead to lower confidence and slow convergence speed for color and geometry fields. As shown in the right figure, those regions will lead to large tracking errors.

the complex geometry regions. So, based on the confidence, we can avoid sampling these regions and use high-reliability and robust pixels to optimize the camera pose during tracking.

Progressive Optimization Weight Function. As shown in [8, 77], NeRF-based pose optimization is sensitive to the initialization. The high-frequency information may lead to suboptimal results when the initial pose is far away from the ground truth. Hence, we propose a progressive weight function that progressively updates the rendering weights during the iteration of the tracking process. Specifically, according to the render function in Sec. 3.2, the distribution of rendering weight is controlled by the δ . Large δ means coarse constraints while small values represent fine-level constraints. So, we apply a coarse-to-fine optimization loss for camera tracking and update δ in a decreasing manner via:

$$\delta = \delta_{max} + (\delta_{min} - \delta_{max}) \sin\left(\frac{i}{N} \cdot \frac{\pi}{2}\right), \quad (17)$$

where i and N are the current and total iteration steps for camera tracking, δ_{min} , δ_{max} are the minimum and maximum values during optimization, and we use the $\sin(\cdot)$ function to update δ non-linearly.

Besides, for tracking, we set the weight of semantic loss as 0, because the predicted semantic results are noisy and inaccurate, and ground RGB and depth images are enough for camera tracking.

3.6 Mapping

We first initialize our permutohedral lattice features and MLP decoders with the first frame $\{I_0, D_0\}$ for several iterations. Then, we perform global bundle adjustments to update our model for every k frame. Following the practice in Co-SLAM [64], we use subset rays to construct the keyframe database instead of storing the whole keyframe [79]. We randomly choose M_m rays from the global keyframe database to perform bundle adjustments using all optimization functions in Sec. 3.4.

4 EXPERIMENTS

In this section, we introduce three commonly used datasets and our experimental setting. When comparing with multiple baselines, we highlight the best three results as **first**, **second**, and **third** for better view.

Dataset. We evaluate our approach on a variety of scenes from three different datasets. For Replica dataset [55], we use the 8 synthetic scenes collected by iMAP [58] for camera tracking and reconstruction evaluation. For the performance on real-world scenes, we use 5 scenes from ScanNet [12] and 3 scenes from TUM RGB-D dataset [56] for pose estimation.

Implementation Details. Our geometry, color, and semantic decoders are implemented as MLP which consists of 2 fully connected (FC) layers with 32 latent dimensional channels. The geometry decoder outputs a 15-dimensional latent feature vector and SDF scalar. We use the ReLU activation function except for the final output. Besides, we apply the Sigmoid function to the output of the color decoder, which limits the color value to (0, 1). We use Adam optimizer and set hyperparameters $\beta = (0.9, 0.999)$, $\epsilon = 1e - 15$. The learning rate for the parameters is set to 0.01. We set the truncation distance tr to 5cm in our method. For the Replica dataset, we use 40 and 100 iterations

Method	Rm0	Rm1	Rm2	Off0	Off1	Off2	Off3	Off4	Avg.
NICE-SLAM [79]	0.97	1.31	1.07	0.88	1.00	1.06	1.10	1.13	1.06
Vox-Fusion [71]	0.40	0.54	0.54	0.50	0.46	0.75	0.50	0.60	0.54
Co-SLAM [64]	0.77	1.04	1.09	0.58	0.53	2.05	1.49	0.84	0.99
ESLAM [23]	0.71	0.70	0.52	0.57	0.55	0.58	0.72	0.63	0.63
Point-SLAM [50]	0.61	0.41	0.37	0.38	0.48	0.54	0.69	0.72	0.52
Ours	0.30	0.40	0.36	0.29	0.31	0.92	0.67	0.44	0.46

Table 1: Tracking Performance on Replica [55] (ATE RMSE \downarrow [cm]). The numbers of compared methods are taken from the original papers or [50, 64].

Method	0000	0059	0106	0169	0207	Avg.
DI-Fusion [20]	62.99	128.00	18.50	75.80	100.19	77.10
iMAP [58]	55.95	32.06	17.50	70.51	11.91	37.59
NICE-SLAM [79]	12.00	14.00	7.90	10.90	6.20	10.20
Vox-Fusion [71]	8.39	9.13	7.44	6.53	5.57	7.41
Co-SLAM [64]	7.18	12.29	9.57	6.62	7.13	8.56
Point-SLAM [50]	10.24	7.81	8.65	22.16	9.54	11.68
Ours	8.70	9.62	8.35	5.64	7.10	7.88

Table 2: Tracking Performance on ScanNet [12] (ATE RMSE \downarrow [cm]). The numbers of all compared methods are taken from the original papers or [50, 64]. The value of Vox-Fusion [71] on 0059 is obtained with their released code. All scenes are evaluated on the 00 trajectory.

for tracking and mapping. For the ScanNet dataset, we use 40 and 50 iterations for tracking and mapping. The loss weights for different optimization components are $\lambda_1=5.0$, $\lambda_2=0.1$, $\lambda_3=1e3$, $\lambda_4=10$, $\lambda_5=1.0$, $\lambda_6=1e-6$. We use [49] to encode the tetrahedron feature, and the multi-resolution tetrahedron features contain 16 level details, each containing a feature vector of 2 dimensions. For positional encoding, we set the frequency to 8, which leads to a 48-dimensional feature vector. So, the final input feature of our system is the concatenated 80 channels feature. The finest tetrahedron resolution is set to 2cm.

4.1 Evaluation of Camera Tracking

In this part, we evaluate the performance of camera tracking on Replica [55], ScanNet [12], and TUM RGB-D [56] datasets. The compared baseline methods, evaluation metrics, and results of this part are shown in the following.

Baselines and Metrics. Following the setting in [50, 64], we take iMAP [58], NICE-SLAM [79], Vox-Fusion [71], Co-SLAM [64], ESLAM [23], and Point-SLAM [50] as the compared baselines. In order to measure the camera tracking accuracy of the proposed method, we use the commonly absolute trajectory error ATE RMSE [57] as the evaluation metric. We align the estimated trajectory and ground truth trajectory using Horn’s closed form solution [19] for a fair comparison.

Qualitative and Quantitative Results. We show the camera tracking performance on the Replica dataset in Tab. 1. As shown by the results, we achieve the best tracking performance across most scenarios, except for the Office 2 scene. Overall, our method outperforms the compared baselines in terms of average results. Besides, to validate

Method	fr1/desk	fr2/xyz	fr3/office	Avg.
DI-Fusion [20]	4.4	2.0	5.8	4.06
NICE-SLAM [79]	4.26	6.19	3.87	4.77
Vox-Fusion [71]	3.52	1.49	26.01	10.34
Co-SLAM [64]	2.70	1.90	2.60	2.50
Point-SLAM [50]	4.34	1.31	3.48	2.40
Ours	2.27	1.63	2.36	2.08

Table 3: Tracking Performance on TUM RGB-D [56] (ATE RMSE \downarrow [cm]). The numbers of compared methods are taken from [50, 64].

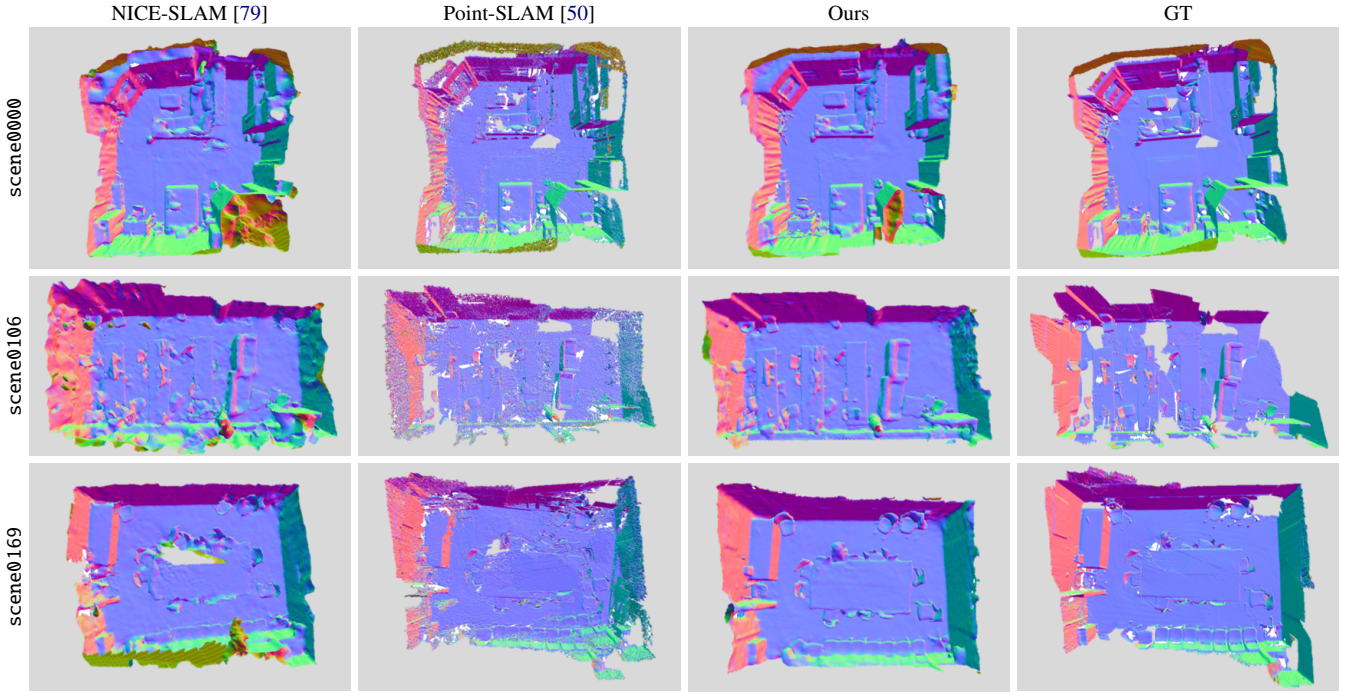


Fig. 5: Reconstruction Results on ScanNet [12]. Compared to the baselines, our method can reconstruct more accurate detailed geometry and generate more complete, smoother mesh.



Fig. 6: Object reconstruction of Replica [55]. We show some selected objects for comparison with vMAP [26].

the performance on real-world scenes, we conduct experiments on ScanNet [12] and TUM-RGBD [56] datasets. The results are shown in Tab. 2 and Tab. 3, respectively. For TUM-RGBD dataset, only the sequence fr3/xyz achieved third performance. On the rest sequences, our approach achieves the best results, including average data. For ScanNet dataset, our camera tracking performance is slightly worse than Vox-Fusion. The reason why Vox-Fusion can achieve good results is that it performs dense BA for each frame. The running speed of Vox-Fusion is rather slow ($\sim 3s$ per frame). Real-world scenarios often involve complex environments, including depth noise, motion blur, and non-Lambertian materials, which makes the neural radiance field hard to model. Compared to the point or voxel based approaches, our performance of reconstructing high-frequency color information will be slightly worse due to the lack of explicit representation.

4.2 Evaluation of Scene and Object Reconstruction

In this part, we evaluate the performance of scene-level and object-level surface reconstruction on Replica dataset [55] and ScanNet [12]. The compared baseline methods, evaluation metrics, and results of this part are shown in the following.

Baseline and Metrics. For scene-level reconstruction evaluation, we follow the setting in [58, 79], we take iMAP [58], NICE-SLAM [79], Co-SLAM [64], and Point-SLAM [50] as the compared baselines. The meshes of [50, 64] are generated via their open-source codes. For object-level reconstruction evaluation, we take vMAP [26] as the baseline and follow the setting in vMAP. Due to vMAP needing camera pose as input, we use the camera pose generated via our system as the input of vMAP for a fair comparison.

For the evaluation metrics, we evaluate the generated meshes on Accuracy (cm), Completion (cm), and Completion ratio (%) with a threshold of 5cm. Specifically, we sample points P and Q from the reconstructed and ground truth meshes and compute the average distance between a point in one set and its nearest point in the other set. For scene-level and object-level reconstruction evaluation, we sample 200000 and 10000 points, respectively.

Qualitative and Quantitative Results. Tab. 4 shows the quantitative scene-level reconstruction comparison results on the Replica dataset [55]. The results of iMAP and NICE-SLAM are taken from the reported value in [79]. The mesh results of Co-SLAM and Point-SLAM are obtained via their open-source codes. Please note that

Method	Metric	Room0	Room1	Room2	Office0	Office1	Office2	Office3	Office4	Avg.
iMAP [58]	Acc. [cm]↓	3.58	3.69	4.68	5.87	3.71	4.81	4.27	4.83	4.43
	Comp. [cm]↓	5.06	4.87	5.51	6.11	5.26	5.65	5.45	6.59	5.56
	Comp. Ratio [< 5cm %]↑	83.91	83.45	75.53	77.71	79.64	77.22	77.34	77.63	79.06
NICE-SLAM [79]	Acc. [cm]↓	2.97	3.23	3.46	5.47	3.33	4.40	3.55	2.87	3.66
	Comp. [cm]↓	3.30	3.07	3.75	4.54	3.83	3.90	4.49	3.91	3.85
	Comp. Ratio [< 5cm %]↑	89.51	86.01	81.14	85.27	88.01	82.61	79.49	85.33	84.67
Co-SLAM [64]	Acc. [cm]↓	1.61	1.31	1.55	1.33	1.11	1.83	1.97	1.73	1.56
	Comp. [cm]↓	2.96	2.46	2.36	1.43	1.82	3.26	3.26	3.36	2.61
	Comp. Ratio [< 5cm %]↑	91.12	92.18	91.44	95.65	93.56	88.53	87.67	87.76	90.99
Point-SLAM [50]	Acc. [cm]↓	1.45	1.14	1.19	1.05	0.86	1.31	1.57	1.51	1.26
	Comp. [cm]↓	3.46	3.02	2.65	1.65	2.21	3.62	3.47	3.90	3.00
	Comp. Ratio [< 5cm %]↑	88.48	89.44	90.13	93.39	90.51	86.17	86.00	85.74	88.73
Ours	Acc. [cm]↓	1.54	1.25	1.41	1.20	1.09	1.58	2.16	1.60	1.48
	Comp. [cm]↓	2.81	2.37	2.23	1.37	1.67	2.86	2.98	3.24	2.44
	Comp. Ratio [< 5cm %]↑	92.14	92.88	92.98	97.13	95.08	90.87	90.17	88.67	92.49

Table 4: Reconstruction Performance on Replica [55]. For NICE-SLAM and iMAP, we take the number from [79]. For Point-SLAM [50] and Co-SLAM [64], we generate the mesh with their open-source codes.

Method	Metric	Room0	Room1	Room2	Office0	Office1	Office2	Office3	Office4	Avg.
vMAP [26]	Object Acc. [cm]↓	3.50	3.06	3.37	2.45	3.04	3.07	3.18	3.07	3.09
	Object Comp. [cm]↓	3.10	3.84	7.11	3.43	1.47	3.93	4.94	9.33	4.64
	Object Comp. Ratio [< 5cm %]↑	84.02	88.32	61.84	69.66	94.58	82.52	77.97	62.45	77.67
Ours	Object Acc. [cm]↓	2.05	1.47	2.87	1.96	1.27	1.84	2.15	2.76	2.04
	Object Comp. [cm]↓	3.50	3.37	4.87	2.62	1.39	3.46	4.41	7.87	3.94
	Object Comp. Ratio [< 5cm %]↑	80.75	87.75	73.21	88.05	95.29	85.27	76.12	65.92	81.52

Table 5: Object Reconstruction Performance on Replica [55]. We reconstruct the object with the pose estimate by ourselves. The numbers of vMAP [26] are evaluated on the meshes obtained from their code with the same pose of ours.

Co-SLAM [64] manually selected additional virtual camera views to assist mesh culling, and we can’t obtain their virtual camera pose. So, we use the same strategy [79] for the meshes generated by Co-SLAM, which leads to better Accuracy (cm) and worse Completion (cm), and Completion ratio (%) than it reported. Besides, Point-SLAM [50] generates mesh using TSDF-Fusion [13], which leads to a more sparse surface. So, their Accuracy is relatively better than other approaches, but with worse Completion ratio metrics.

As can be seen from the results in Tab. 4, our method achieves better or comparable reconstruction performance, thanks to the accurate camera pose estimation and the inherent smoothness provided by our tetrahedron-based parametric encoding. We achieved the best results on the Completion (cm), and Completion ratio metrics. Compared with the second-best approach, we achieved 6.9%, and 1.6% performance improvement on the average results, respectively. The performance of our approach on Accuracy (cm) metric is only slightly worse than Point-SLAM [50], because [50] uses TSDF-Fusion [13] as the post-process to obtain the mesh. Among those methods whose meshes are generated via marching cubes [33], we achieve the best performance on Accuracy (cm) metric. Additionally, we show some qualitative comparison results of Replica and ScanNet datasets in the Fig. 8 and Fig. 5, respectively. The geometry results in Fig. 8 are rendered from novel camera views of three selected Replica scenes. Our method can restore surface details well and complete the observation area. The results in Fig. 5 are rendered from the top view to show the overall reconstruction results of the whole scene. As can be seen, compared with NICE-SLAM [79] and Point-SLAM [50], we can reconstruct a more watertight, smoother surface for the back side and unobserved areas.

For object-level reconstruction, we compared with vMAP [26] on the Replica dataset. Because vMAP [26] needs the camera poses as the input, we use the camera pose recovered by our system as the input of vMAP for a fair comparison. The quantitative comparison results are shown in Tab. 5. As can be seen from the table, we achieve the best results on object-level reconstruction. The decoder parameters of vMAP are approximately N times greater than ours, where N is

the number of objects in the scene, as it allocates separate network parameters for each object. Despite using fewer parameters, we can still estimate the camera pose and achieve comparable reconstruction results.

Method	Acc.(%)	Avg.Acc.(%)	mIOU(%)	fwIOU(%)
Haghighi * [17]	98.47	94.14	82.61	97.22
Ours *	99.09	97.95	98.55	98.20
Mask2Former [9]	78.84	75.66	68.20	72.75
Ours w/o Fusion	82.47	80.11	69.53	75.48
Ours	84.88	82.76	70.68	76.72

Table 6: Semantic Segmentation Performance on Replica [55]. The symbol * denotes the results obtained with ground truth semantic labels. The numbers of [17] are taken from their paper.

4.3 Evaluation of Semantic Segmentation

In this part, we evaluate the performance of semantic segmentation on the Replica dataset [55]. The compared baseline methods, evaluation metrics, and results of this part are shown in the following.

Baseline and Metrics. For the evaluation of semantic segmentation, we take Haghighi *et al.* [17] as the comparison baseline. The ground truth semantic labels for Replica [55] are rendered with Habitat [34] with the original trajectory. Besides, we map the label set following the setting in [9, 54] for semantic segmentation evaluation. And following the setting of [17], we use four commonly used metrics: Total Accuracy (%), Avg. Accuracy (%), mIOU (%), and fwIOU (%). Besides, we also compare the learned semantic results of our 3D semantic field with the 2D semantic segmentation model Mask2Former [9].

Qualitative and Quantitative Results. Due to the lack of open-source code for [17], we conducted semantic experiments and comparisons on four scenes (Room 0, Room 1, Room 2, Office 0) based on their settings [17]. The results of average metrics are shown in the top part of Tab. 6. The symbol * denotes the segmentation results obtained

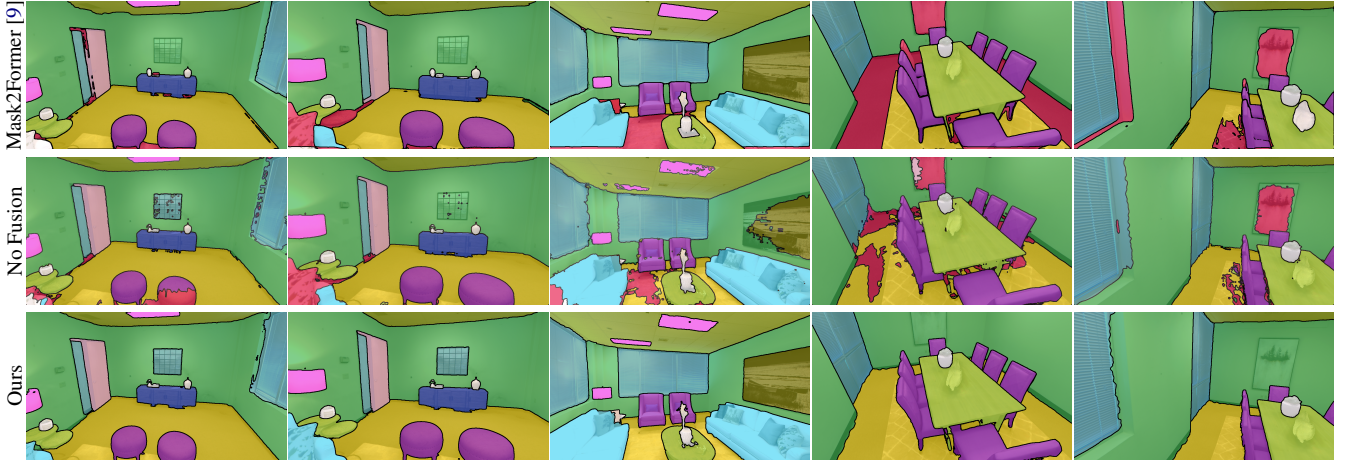


Fig. 7: Semantic Segmentation Results on Replica [55]. We show the multi-view segmentation results of different approaches. The top, middle, and bottom parts show the segmentation results of Mask2Former [9], our approach without semantic fusion, and our approach with semantic fusion respectively. Comparing the segmentation results from different views, we can see that our method can learn more consistent semantic representation.

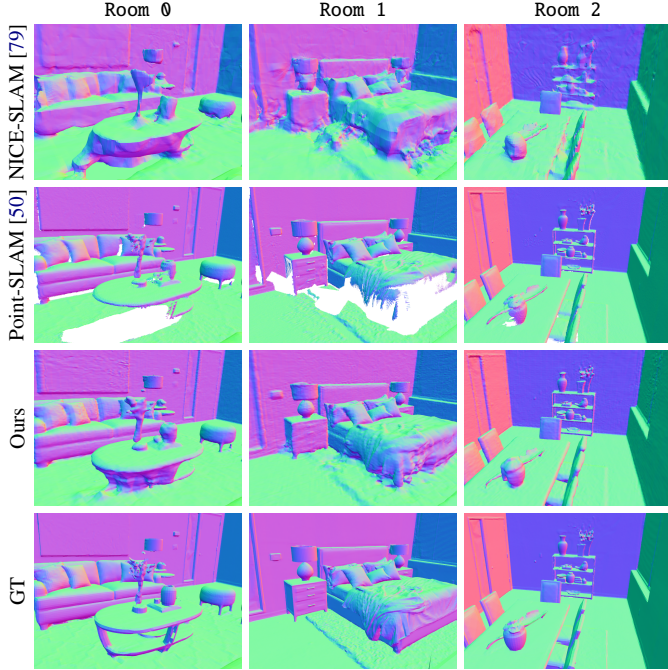


Fig. 8: Reconstruction Performance on Replica [55]. We show the novel view rendering results of the reconstructed mesh.

with the supervision of semantic annotation of [55], which is the same to [17]. As can be seen, we outperform [17] on all averaged metrics of 4 scenes. Especially, for the metric mIOU, we achieve a significant improvement over [17] (82.61% v.s. 98.55%).

Besides, we also test the performance with 2D noise inputs which are generated by Mask2Former [9] for all scenes. As shown in the bottom of Tab. 6, compared to the noise 2D segmentation, our approach can improve the multi-view semantic consistency, which leads to 3D consistent semantic representation. Those quantitative experimental results verify that our approach can learn 3D consistent semantic information from 2D noisy and multi-view inconsistent segmentation results. Additionally, we also show some qualitative semantic segmentation results in Fig. 7. We show the segmentation results of different views to validate the consistency. The first row shows different view segmentation results from Mask2Former [9], the second row shows the

results generated by our approaches without semantic fusion (Sec. 3.3), and the third row shows the results generated by our approaches. As shown in the figure, the results generated by Mask2Former usually contain multi-view inconsistency, e.g. complex edges of furniture, or ambiguous areas. Under different viewpoints, the same object or region would be recognized as different categories (different colors represent different categories). Those noisy and inconsistent semantic observations can lead to unstable or conflicting 3D semantic information learning without any process. For example, the segmentation results in the middle row usually contain a lot of noise and semantic inconsistent areas. For the performance of our approach (the third row), even with noisy input data, our method can still produce 3D spatially consistent semantic segmentation results across different views.

4.4 Ablation Study

In this part, we perform the ablation study to investigate the effect of each part in our system.

Experiment	Room 1		Office 1	
	Acc.[cm]↓	Comp.[cm]↓	Acc.[cm]↓	Comp.[cm]↓
Only PE	3.42	3.78	3.16	4.61
+ Cube	1.30	2.48	1.14	1.88
+ Tetrahedron	1.25	2.37	1.09	1.67

Table 7: Reconstruction performance of using different encoding features.

Effect of Multi-view Semantic Fusion. The bottom part of Tab. 6 shows the performance without multi-view semantic fusion, which is lower than our approach. From the table, we know that without using our strategy, our baseline system can also achieve better semantic segmentation results than Mask2Former [9]. This is because our neural implicit representation can learn 3D consistent representation from noise 2D input, and progressively converge to a global optimal from 2D multi-view observations.

Effect of Using Different Neural Representation. Here, we show the reconstruction performance of using different neural representations for our system. We select two scenes from Replica [55] for evaluation and the results are shown in Tab. 7. As can be seen from the table, without any additional feature encoding, only using PE can lead to a worse reconstruction of the scene. Using additional features can enhance the encoding capacity of MLPs and lead to performance improvement. Besides, we also show the performance of using additional multi-resolution cube-based feature encoding [38]. Compared with the cube representation, our tetrahedron representation can achieve a better surface reconstruction.

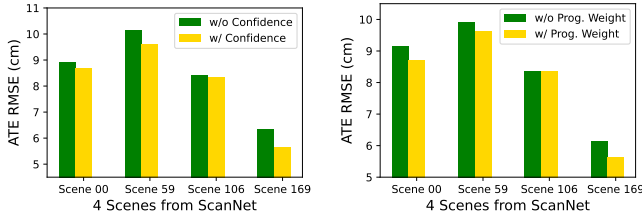


Fig. 9: Tracking Performance on 4 Scenes from ScanNet [12] (ATE RMSE ↓ [cm]). The left and right figures respectively show the effects of using confidence-based pixel sampling and progressive optimization weight during the camera tracking process.

Effect of Confidence-guided Pixel Sampling. Here, we show the results to validate the effectiveness of confidence-based pixel sampling for camera tracking. We select four scenes from ScanNet [12] dataset for evaluation and the results are shown in the left part of Fig. 9. As can be seen from the figure, with the guidance of semantic confidence we can reduce the camera tracking error (ATE RMSE) on the selected scenes. With the help of confidence, we can avoid sampling pixels in the object edges areas and complex geometric regions during the tracking process. The pixels in these areas usually have a relatively slow convergence speed in the mapping process, which will lead to relatively large tracking errors.

Effect of Progressive Optimization Weight. We show the performance of using progressive optimization weight for camera tracking. The comparison results of 4 selected scenes are shown in the right part of Fig. 9. As can be seen from the figure, with progressive optimization weight we can also reduce the camera tracking error (ATE RMSE) on the selected scenes. The progressive weight can lead to a coarse-to-fine optimization manner and avoid the model falling into local minima.

4.5 Memory and Running Time

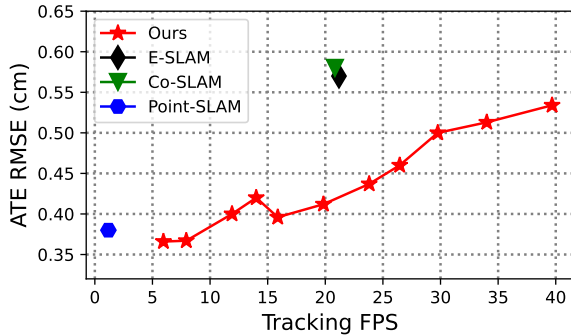


Fig. 10: Tracking speed (FPS) and error (ATE RMSE) of different approaches. We use different tracking iterations to obtain the ATE RMSE error curve at different tracking FPS.

In this part, we show the memory usage and runtime performance of our approach on the Replica dataset.

For the memory usage of our system, the whole training parameters of our system are three MLP decoders $\{\mathcal{M}_{geo}, \mathcal{M}_{rgb}, \mathcal{M}_{sem}\}$ and multi-resolution tetrahedron features Θ . For example, on scene Office 0, the whole parameters of MLP decoders and embedding features are 8.02MB (0.02MB + 8.00MB), which is much less than the parameters of Point-SLAM, 27.74MB (0.51MB + 27.23MB). For the running speed of our system, we show the camera tracking FPS with respect to the ATE RMSE (cm) on the Replica dataset. We perform global bundle adjustments for 10 iterations when a new keyframe comes, and use 5-50 iterations for camera tracking. The tracking FPS results with different tracking iterations are shown in Fig. 10. The runtimes are profiled on a single NVidia RTX 4090 card. We can achieve good tracking

performance at the ~30 tracking FPS with about 0.5 cm tracking error. Additionally, we also show the performance of ESLAM [23], Co-SLAM [64], and Point-SLAM [50] in the figure. Compared to ESLAM and Co-SLAM, we can achieve better camera tracking accuracy at the same speed. Compared to Point-SLAM, we can achieve faster tracking speed with comparable tracking performance.



Fig. 11: The AR demo on scene Office 4 from Replica [55]. The top-left is the original scene image, and on the right are three AR objects and the logo of ISMAR 2024. We render those objects in the original scene with the camera pose estimated by our approach. The rendered results are shown in the lower left. For more AR demo videos, please refer to our supplementary material.

4.6 AR Application

In this part, we show the application of our system in AR. Our system can not only localize the pose of the camera but also reconstruct watertight scene geometry/depth and perform novel view synthesis via our implicit representation. Therefore, our method can be very suitable for VR/AR applications. We demonstrate an AR example, as shown in Fig. 11. The scene image is selected from Office 4 of Replica [55] dataset. We place three virtual objects and one ISMAR 2024 logo (shown on the right of the figure) into reconstructed scenes according to the pose and depth recovered by our system. The rendered AR image is shown at the bottom of Fig. 11, and we highlighted the virtual objects and logo with red boxes. We can accurately represent the occlusion relationship between real and virtual contents via our accurate camera pose and rendered dense depth map. For the multi-view AR demo, please refer to our supplementary video, which shows we can handle occlusion between different objects very well.

5 CONCLUSION

In this paper, we present NIS-SLAM, a neural implicit dense semantic RGB-D SLAM that can model consistent semantic information from inconsistent segmentation results generated by a pre-trained 2D CNN. For high-fidelity surface reconstruction and spatial consistent scene understanding, we use a hybrid representation of high-frequency multi-resolution tetrahedron features and low-frequency positional encoding for our system. And the multi-view semantic fusion is proposed to handle the inconsistency of 2D segmentation results. Besides, the semantic guided pixel sampling and progressive optimization weight are used for robust camera tracking. Extensive experiments on a variety of datasets have shown the effectiveness and application of our proposed system.

Currently, the proposed NIS-SLAM approach relies on the segmentation results of a close-set model, which limits its applications for open-set world tasks. Combined with the large language/open-set models may be more practical for many applications. Compared to methods with explicit representation (point, 3D Gaussian), our approach cannot recover high-frequency information well.

6 ACKNOWLEDGMENTS

This work was partially supported by NSF of China (No.61932003).

REFERENCES

- [1] K. S. Arun, T. S. Huang, and S. D. Blostein. Least-squares fitting of two 3-d point sets. *IEEE Transactions on Pattern Analysis and Machine Intelligence*, PAMI-9(5):698–700, 1987. 1, 2
- [2] D. Azinović, R. Martin-Brualla, D. B. Goldman, M. Nießner, and J. Thies. Neural RGB-D surface reconstruction. In *IEEE/CVF Conference on Computer Vision and Pattern Recognition*, pp. 6290–6301, 2022. 2, 3, 4
- [3] M. Bloesch, J. Czarowski, R. Clark, S. Leutenegger, and A. J. Davison. CodeSLAM - learning a compact, optimisable representation for dense visual SLAM. In *IEEE/CVF Conference on Computer Vision and Pattern Recognition*, pp. 2560–2568, 2018. 1, 2
- [4] K. Blomqvist, L. Ott, J. J. Chung, and R. Siegwart. Baking in the feature: Accelerating volumetric segmentation by rendering feature maps. *CoRR*, abs/2209.12744, 2022. 3
- [5] C. Campos, R. Elvira, J. J. G. Rodríguez, J. M. M. Montiel, and J. D. Tardós. ORB-SLAM3: an accurate open-source library for visual, visual-inertial, and multimap SLAM. *IEEE Trans. Robotics*, 37(6):1874–1890, 2021. 2
- [6] A. Chen, Z. Xu, A. Geiger, J. Yu, and H. Su. Tensorf: Tensorial radiance fields. In *European Conference on Computer Vision (ECCV)*, 2022. 2
- [7] D. Chen, H. Li, W. Ye, Y. Wang, W. Xie, S. Zhai, N. Wang, H. Liu, H. Bao, and G. Zhang. Pgsr: Planar-based gaussian splatting for efficient and high-fidelity surface reconstruction. 2024. 2
- [8] Y. Chen, X. Chen, X. Wang, Q. Zhang, Y. Guo, Y. Shan, and F. Wang. Local-to-global registration for bundle-adjusting neural radiance fields. In *IEEE/CVF Conference on Computer Vision and Pattern Recognition*, pp. 8264–8273, 2023. 5
- [9] B. Cheng, I. Misra, A. G. Schwing, A. Kirillov, and R. Girdhar. Masked-attention mask transformer for universal image segmentation. In *IEEE Conference on Computer Vision and Pattern Recognition*, 2022. 2, 3, 4, 7, 8
- [10] C. Chung, Y. Tseng, Y. Hsu, X. Q. Shi, Y. Hua, J. Yeh, W. Chen, Y. Chen, and W. H. Hsu. Orbeez-SLAM: A real-time monocular visual SLAM with ORB features and nerf-realized mapping. *CoRR*, abs/2209.13274, 2022. 2
- [11] B. Curless and M. Levoy. A volumetric method for building complex models from range images. In *Proceedings of annual conference on Computer graphics and interactive techniques*, pp. 303–312, 1996. 1, 2
- [12] A. Dai, A. X. Chang, M. Savva, M. Halber, T. Funkhouser, and M. Nießner. ScanNet: Richly-annotated 3D reconstructions of indoor scenes. In *IEEE Conference on Computer Vision and Pattern Recognition*, pp. 2432–2443, 2017. 2, 5, 6, 9
- [13] A. Dai, M. Nießner, M. Zollhöfer, S. Izadi, and C. Theobalt. BundleFusion: Real-time globally consistent 3D reconstruction using on-the-fly surface reintegration. *ACM Trans. Graph.*, 36(3):24:1–24:18, 2017. 1, 2, 7
- [14] X. Fu, S. Zhang, T. Chen, Y. Lu, L. Zhu, X. Zhou, A. Geiger, and Y. Liao. Panoptic nerf: 3d-to-2d label transfer for panoptic urban scene segmentation. In *International Conference on 3D Vision*, pp. 1–11, 2022. 1
- [15] C. Gao, A. Saraf, J. Kopf, and J.-B. Huang. Dynamic view synthesis from dynamic monocular video. In *IEEE/CVF International Conference on Computer Vision*, pp. 5712–5721, 2021. 2
- [16] M. Grinvald, F. Furrer, T. Novkovic, J. J. Chung, C. Cadena, R. Siegwart, and J. Nieto. Volumetric Instance-Aware Semantic Mapping and 3D Object Discovery. *IEEE Robotics and Automation Letters*, 4(3):3037–3044, 2019. 2
- [17] Y. Haghighi, S. Kumar, J. P. Thiran, and L. Van Gool. Neural implicit dense semantic slam. *arXiv preprint arXiv:2304.14560*, 2023. 1, 2, 7, 8
- [18] M. Han, Z. Zhang, Z. Jiao, X. Xie, Y. Zhu, S.-C. Zhu, and H. Liu. Reconstructing interactive 3d scenes by panoptic mapping and cad model alignments. In *IEEE International Conference on Robotics and Automation*, pp. 12199–12206, 2021. 2
- [19] B. K. Horn, H. M. Hilden, and S. Negahdaripour. Closed-form solution of absolute orientation using orthonormal matrices. *JOSA A*, 5(7):1127–1135, 1988. 5
- [20] J. Huang, S.-S. Huang, H. Song, and S.-M. Hu. Di-fusion: Online implicit 3d reconstruction with deep priors. In *IEEE/CVF Conference on Computer Vision and Pattern Recognition*, pp. 8932–8941, 2021. 1, 2, 5
- [21] M. Jaderberg, K. Simonyan, A. Zisserman, et al. Spatial transformer networks. *Advances in neural information processing systems*, 28, 2015. 4
- [22] C. Jiang, H. Zhang, P. Liu, Z. Yu, H. Cheng, B. Zhou, and S. Shen. H2-Mapping: Real-time dense mapping using hierarchical hybrid representation. *arXiv preprint arXiv:2306.03207*, 2023. 1, 2
- [23] M. M. Johari, C. Carta, and F. Fleuret. ESLAM: Efficient dense slam system based on hybrid representation of signed distance fields. In *IEEE/CVF Conference on Computer Vision and Pattern Recognition*, 2023. 1, 2, 3, 5, 9
- [24] J. T. Kajiya and B. V. Herzen. Ray tracing volume densities. In *SIGGRAPH*, pp. 165–174, 1984. 1
- [25] B. Kerbl, G. Kopanas, T. Leimkühler, and G. Drettakis. 3d gaussian splatting for real-time radiance field rendering. *ACM Transactions on Graphics*, 42(4), 2023. 2
- [26] X. Kong, S. Liu, M. Taher, and A. J. Davison. vmap: Vectorised object mapping for neural field slam. In *IEEE/CVF Conference on Computer Vision and Pattern Recognition*, pp. 952–961, 2023. 2, 6, 7
- [27] J. Kulháněk and T. Sattler. Tetra-nerf: Representing neural radiance fields using tetrahedra. In *IEEE/CVF International Conference on Computer Vision*, pp. 18412–18423, 2023. 2, 3
- [28] A. Kundu, K. Genova, X. Yin, A. Fathi, C. Pantofaru, L. J. Guibas, A. Tagliasacchi, F. Dellaert, and T. Funkhouser. Panoptic neural fields: A semantic object-aware neural scene representation. In *IEEE/CVF Conference on Computer Vision and Pattern Recognition*, pp. 12871–12881, 2022. 1
- [29] H. Li, T. Fan, H. Zhai, Z. Cui, H. Bao, and G. Zhang. Bdlloc: Global localization from 2.5d building map. In *IEEE International Symposium on Mixed and Augmented Reality*, pp. 80–89, 2021. 1
- [30] H. Li, X. Yang, H. Zhai, Y. Liu, H. Bao, and G. Zhang. Vox-surf: Voxel-based implicit surface representation. *IEEE Trans. Vis. Comput. Graph.*, 30(3):1743–1755, 2024. 2
- [31] H. Li, H. Zhai, X. Yang, Z. Wu, Y. Zheng, H. Wang, J. Wu, H. Bao, and G. Zhang. Imtooth: Neural implicit tooth for dental augmented reality. *IEEE Trans. Vis. Comput. Graph.*, 29(5):2837–2846, 2023. 2
- [32] L. Liu, J. Gu, K. Z. Lin, T. Chua, and C. Theobalt. Neural sparse voxel fields. In *Annual Conference on Neural Information Processing Systems*, 2020. 2
- [33] W. E. Lorensen and H. E. Cline. Marching cubes: A high resolution 3d surface construction algorithm. In *Seminal graphics: pioneering efforts that shaped the field*, pp. 347–353, 1998. 7
- [34] Manolis Savva*, Abhishek Kadian*, Oleksandr Maksymets*, Y. Zhao, E. Wijmans, B. Jain, J. Straub, J. Liu, V. Koltun, J. Malik, D. Parikh, and D. Batra. Habitat: A Platform for Embodied AI Research. In *IEEE/CVF International Conference on Computer Vision*, 2019. 7
- [35] R. Martin-Brualla, N. Radwan, M. S. Sajjadi, J. T. Barron, A. Dosovitskiy, and D. Duckworth. Nerf in the wild: Neural radiance fields for unconstrained photo collections. In *IEEE/CVF Conference on Computer Vision and Pattern Recognition*, pp. 7210–7219, 2021. 2
- [36] J. McCormac, A. Handa, A. Davison, and S. Leutenegger. Semanticfusion: Dense 3d semantic mapping with convolutional neural networks. In *IEEE International Conference on Robotics and Automation*, pp. 4628–4635, IEEE, 2017. 2
- [37] B. Mildenhall, P. P. Srinivasan, M. Tancik, J. T. Barron, R. Ramamoorthi, and R. Ng. Nerf: Representing scenes as neural radiance fields for view synthesis. In *European Conference on Computer Vision*, 2020. 1, 2, 3
- [38] T. Müller, A. Evans, C. Schied, and A. Keller. Instant neural graphics primitives with a multiresolution hash encoding. *ACM Trans. Graph.*, 41(4):102:1–102:15, 2022. 2, 3, 8
- [39] J. Munkberg, J. Hasselgren, T. Shen, J. Gao, W. Chen, A. Evans, T. Müller, and S. Fidler. Extracting triangular 3d models, materials, and lighting from images. In *IEEE/CVF Conference on Computer Vision and Pattern Recognition*, pp. 8280–8290, 2022. 2
- [40] R. Mur-Artal and J. D. Tardós. ORB-SLAM2: an open-source SLAM system for monocular, stereo, and RGB-D cameras. *IEEE Trans. Robotics*, 33(5):1255–1262, 2017. 2
- [41] G. Narita, T. Seno, T. Ishikawa, and Y. Kaji. Panopticfusion: Online volumetric semantic mapping at the level of stuff and things. In *IEEE/RSJ International Conference on Intelligent Robots and Systems*, pp. 4205–4212, 2019. 2
- [42] R. A. Newcombe, S. Izadi, O. Hilliges, D. Molyneaux, D. Kim, A. J. Davison, P. Kohli, J. Shotton, S. Hodges, and A. Fitzgibbon. KinectFusion: real-time dense surface mapping and tracking. In *IEEE International Symposium on Mixed and Augmented Reality*, pp. 127–136, 2011. 1, 2
- [43] R. A. Newcombe, S. J. Lovegrove, and A. J. Davison. Dtm: Dense tracking and mapping in real-time. In *IEEE/CVF International Conference on Computer Vision*, pp. 2320–2327, 2011. 2
- [44] M. Oechsle, S. Peng, and A. Geiger. UNISURF: unifying neural implicit surfaces and radiance fields for multi-view reconstruction. In *IEEE/CVF International Conference on Computer Vision*, pp. 5569–5579, 2021. 2

- [45] K. Park, U. Sinha, J. T. Barron, S. Bouaziz, D. B. Goldman, S. M. Seitz, and R. Martin-Brualla. Nerfies: Deformable neural radiance fields. In *IEEE/CVF International Conference on Computer Vision*, pp. 5865–5874, 2021. 2
- [46] K. Park, U. Sinha, P. Hedman, J. T. Barron, S. Bouaziz, D. B. Goldman, R. Martin-Brualla, and S. M. Seitz. Hypernerf: A higher-dimensional representation for topologically varying neural radiance fields. *arXiv preprint arXiv:2106.13228*, 2021. 2
- [47] A. Pumarola, E. Corona, G. Pons-Moll, and F. Moreno-Noguer. D-nerf: Neural radiance fields for dynamic scenes. In *IEEE/CVF Conference on Computer Vision and Pattern Recognition*, pp. 10318–10327, 2021. 2
- [48] A. Rosinol, J. J. Leonard, and L. Carlone. NeRF-SLAM: Real-time dense monocular SLAM with neural radiance fields. *CoRR*, abs/2210.13641, 2022. 2
- [49] R. A. Rosu and S. Behnke. Permutosdf: Fast multi-view reconstruction with implicit surfaces using permutohedral lattices. In *IEEE/CVF Conference on Computer Vision and Pattern Recognition*, 2023. 2, 3, 5
- [50] E. Sandström, Y. Li, L. Van Gool, and M. R. Oswald. Point-slam: Dense neural point cloud-based slam. In *IEEE/CVF International Conference on Computer Vision*, 2023. 1, 2, 3, 5, 6, 7, 8, 9
- [51] T. Schöps, T. Sattler, and M. Pollefeys. BAD SLAM: bundle adjusted direct RGB-D SLAM. In *IEEE/CVF Conference on Computer Vision and Pattern Recognition*, pp. 134–144, 2019. 2
- [52] Z. Shan, R. Li, and S. Schwertfeger. Rgb-d-inertial trajectory estimation and mapping for ground robots. *Sensors*, 19(10):2251, 2019. 2
- [53] T. Shen, J. Gao, K. Yin, M. Liu, and S. Fidler. Deep marching tetrahedra: a hybrid representation for high-resolution 3d shape synthesis. In *Advances in Neural Information Processing Systems*, pp. 6087–6101, 2021. 2, 3
- [54] Y. Siddiqui, L. Porzi, S. R. Bulò, N. Müller, M. Nießner, A. Dai, and P. Kotschieder. Panoptic lifting for 3d scene understanding with neural fields. In *IEEE/CVF Conference on Computer Vision and Pattern Recognition*, pp. 9043–9052, 2023. 1, 7
- [55] J. Straub, T. Whelan, L. Ma, Y. Chen, E. Wijmans, S. Green, J. J. Engel, R. Mur-Artal, C. Ren, S. Verma, A. Clarkson, M. Yan, B. Budge, Y. Yan, X. Pan, J. Yon, Y. Zou, K. Leon, N. Carter, J. Briales, T. Gillingham, E. Mueggler, L. Pesqueira, M. Savva, D. Batra, H. M. Strasdat, R. D. Nardi, M. Goesele, S. Lovegrove, and R. Newcombe. The Replica dataset: A digital replica of indoor spaces. *arXiv preprint arXiv:1906.05797*, 2019. 2, 5, 6, 7, 8, 9
- [56] J. Sturm, N. Engelhard, F. Endres, W. Burgard, and D. Cremers. A benchmark for the evaluation of RGB-D SLAM systems. In *IEEE/RSJ International Conference on Intelligent Robots and Systems*, pp. 573–580, 2012. 5, 6
- [57] J. Sturm, N. Engelhard, F. Endres, W. Burgard, and D. Cremers. A benchmark for the evaluation of rgb-d slam systems. In *IEEE/RSJ international conference on intelligent robots and systems*, pp. 573–580, 2012. 5
- [58] E. Sucar, S. Liu, J. Ortiz, and A. J. Davison. iMAP: Implicit mapping and positioning in real-time. In *IEEE/CVF International Conference on Computer Vision*, pp. 6209–6218. IEEE, 2021. 1, 2, 3, 4, 5, 6, 7
- [59] J. Sun, Y. Xie, L. Chen, X. Zhou, and H. Bao. NeuralRecon: Real-time coherent 3D reconstruction from monocular video. In *IEEE/CVF Conference on Computer Vision and Pattern Recognition*, 2021. 2
- [60] M. Tancik, V. Casser, X. Yan, S. Pradhan, B. P. Mildenhall, P. P. Srinivasan, J. T. Barron, and H. Kretschmar. Block-nerf: Scalable large scene neural view synthesis. In *IEEE/CVF Conference on Computer Vision and Pattern Recognition*, pp. 8238–8248, 2022. 2
- [61] K. Tateno, F. Tombari, I. Laina, and N. Navab. Cnn-slam: Real-time dense monocular slam with learned depth prediction. In *IEEE/CVF Conference on Computer Vision and Pattern Recognition*, pp. 6243–6252, 2017. 2
- [62] Z. Teed and J. Deng. DROID-SLAM: deep visual SLAM for monocular, stereo, and RGB-D cameras. In *Annual Conference on Neural Information Processing Systems*, pp. 16558–16569, 2021. 1, 2
- [63] H. Turki, D. Ramanan, and M. Satyanarayanan. Mega-nerf: Scalable construction of large-scale nerfs for virtual fly-throughs. In *IEEE/CVF Conference on Computer Vision and Pattern Recognition*, pp. 12912–12921, 2022. 2
- [64] H. Wang, J. Wang, and L. Agapito. Co-SLAM: joint coordinate and sparse parametric encodings for neural real-time slam. In *IEEE/CVF international conference on Computer Vision and Pattern Recognition*, 2023. 1, 2, 3, 5, 6, 7, 9
- [65] P. Wang, L. Liu, Y. Liu, C. Theobalt, T. Komura, and W. Wang. NeuS: Learning neural implicit surfaces by volume rendering for multi-view reconstruction. In *Annual Conference on Neural Information Processing Systems 2021*, pp. 27171–27183, 2021. 2, 3
- [66] S. Weder, J. L. Schonberger, M. Pollefeys, and M. R. Oswald. Neurfusion: Online depth fusion in latent space. In *IEEE/CVF Conference on Computer Vision and Pattern Recognition*, pp. 3162–3172, 2021. 1, 2
- [67] Y. Wei, M. Liu, H. Wang, R. Zhu, G. Hu, and W. Zuo. Learning flow-based feature warping for face frontalization with illumination inconsistent supervision. In *Proceedings of the European Conference on Computer Vision*, 2020. 4
- [68] T. Whelan, M. Kaess, M. Fallon, H. Johannsson, J. Leonard, and J. McDonald. Kintinuous: Spatially extended kinectfusion. In *Proceedings of RSS '12 Workshop on RGB-D: Advanced Reasoning with Depth Cameras*, 2012. 1
- [69] T. Whelan, R. F. Salas-Moreno, B. Glocker, A. J. Davison, and S. Leutenegger. ElasticFusion: Real-time dense SLAM and light source estimation. In *International Journal of Robotics Research*, vol. 35, pp. 1697–1716, 2016. 2
- [70] Q. Xu, Z. Xu, J. Philip, S. Bi, Z. Shu, K. Sunkavalli, and U. Neumann. Point-nerf: Point-based neural radiance fields. In *IEEE/CVF Conference on Computer Vision and Pattern Recognition*, pp. 5438–5448, 2022. 2
- [71] X. Yang, H. Li, H. Zhai, Y. Ming, Y. Liu, and G. Zhang. Vox-Fusion: Dense tracking and mapping with voxel-based neural implicit representation. In *IEEE International Symposium on Mixed and Augmented Reality*, pp. 499–507, 2022. 1, 2, 3, 4, 5
- [72] H. Zhai, H. Li, X. Yang, G. Huang, Y. Ming, H. Bao, and G. Zhang. Vox-fusion++: Voxel-based neural implicit dense tracking and mapping with multi-maps. *arXiv preprint arXiv:2403.12536*, 2024. 2
- [73] Y. Zhang, F. Tosi, S. Mattoccia, and M. Poggi. Go-slam: Global optimization for consistent 3d instant reconstruction. In *IEEE/CVF International Conference on Computer Vision*, pp. 3727–3737, 2023. 2
- [74] S. Zhi, T. Laidlow, S. Leutenegger, and A. J. Davison. In-place scene labelling and understanding with implicit scene representation. In *IEEE/CVF International Conference on Computer Vision*, pp. 15838–15847, 2021. 1
- [75] T. Zhou, M. Brown, N. Snavely, and D. G. Lowe. Unsupervised learning of depth and ego-motion from video. In *IEEE/CVF conference on computer vision and pattern recognition*, pp. 1851–1858, 2017. 4
- [76] S. Zhu, G. Wang, H. Blum, J. Liu, L. Song, M. Pollefeys, and H. Wang. Sni-slam: Semantic neural implicit slam. In *Proceedings of the IEEE/CVF Conference on Computer Vision and Pattern Recognition*, pp. 21167–21177, 2024. 2
- [77] Z. Zhu, Y. Chen, Z. Wu, C. Hou, Y. Shi, C. Li, P. Li, H. Zhao, and G. Zhou. Latitude: Robotic global localization with truncated dynamic low-pass filter in city-scale nerf. In *IEEE International Conference on Robotics and Automation*, pp. 8326–8332, 2023. 5
- [78] Z. Zhu, S. Peng, V. Larsson, Z. Cui, M. R. Oswald, A. Geiger, and M. Pollefeys. NICER-SLAM: neural implicit scene encoding for RGB SLAM. *CoRR*, abs/2302.03594, 2023. 1, 2
- [79] Z. Zhu, S. Peng, V. Larsson, W. Xu, H. Bao, Z. Cui, M. R. Oswald, and M. Pollefeys. NICE-SLAM: neural implicit scalable encoding for SLAM. In *IEEE Conference on Computer Vision and Pattern Recognition*, pp. 12786–12796, 2022. 1, 2, 3, 5, 6, 7, 8